Title
Attenuation correction for small animal PET tomographs

Permalink
https://escholarship.org/uc/item/41n377p3

Journal
Physics in Medicine and Biology, 50(8)

ISSN
0031-9155

Authors
Chow, Patrick L
Rannou, Fernando R
Chatziioannou, Arion F

Publication Date
2005-04-21

Peer reviewed

Attenuation correction for small animal PET tomographs

Patrick L Chow[1]**, Fernando R Rannou**[2] **and Arion F Chatziioannou**[1]

[1] David Geffen School of Medicine at UCLA, Crump Institute for Molecular Imaging,
University of California, 700 Westwood Plaza, Los Angeles, CA 90095, USA
[2] Departamento de Ingenieria Informatica, Universidad de Santiago de Chile (USACH),
Av. Ecuador 3659, Santiago, Chile

E-mail: plchow@mednet.ucla.edu

Abstract

Attenuation correction is one of the important corrections required for quantitative positron emission tomography (PET). This work will compare the quantitative accuracy of attenuation correction using a simple global scale factor with traditional transmission-based methods acquired either with a small animal PET or a small animal x-ray computed tomography (CT) scanner. Two phantoms (one mouse-sized and one rat-sized) and two animal subjects (one mouse and one rat) were scanned in CTI Concorde Microsystem's microPET® Focus™ for emission and transmission data and in ImTek's MicroCAT™ II for transmission data. PET emission image values were calibrated against a scintillation well counter. Results indicate that the scale factor method of attenuation correction places the average measured activity concentration about the expected value, without correcting for the cupping artefact from attenuation. Noise analysis in the phantom studies with the PET-based method shows that noise in the transmission data increases the noise in the corrected emission data. The CT-based method was accurate and delivered low-noise images suitable for both PET data correction and PET tracer localization.

1. Introduction

Annihilation photons in positron emission tomography (PET) are subject to attenuation as they travel through the imaged object. This effect reduces the number of photons detected in each line of response. If the material properties of the object are known, the measurement along each line of response can be corrected for this attenuation effect (Huang *et al* 1979). Although the magnitude of this correction for small animal subjects is much smaller than for humans (1.3 for a 3 cm diameter mouse versus 1.6 for a 5 cm diameter rat versus 45 for a 40 cm diameter human), it is important to correct the data for quantitative analysis of the tracer distribution.

Several methods of correcting for attenuation in PET exist (Zaidi and Hasegawa 2003). This work will compare the quantitative accuracy of attenuation correction using a simple global scale factor (Tai *et al* 2005) with traditional transmission-based methods (Huang *et al* 1979, Dahlbom and Hoffman 1987). Transmission images can be acquired either with a PET or an x-ray computed tomography (CT) scanner (Dekemp and Nahmias 1994, Karp *et al* 1995, Kinahan *et al* 1998). In transmission imaging, a photon source with known flux is rotated around the object and the photon attenuation is recorded by either the PET or the CT tomograph. For PET transmission, the source is radioactive while for CT transmission, the source is an x-ray tube.

The main advantage of using a global scale factor for attenuation correction is convenience. No transmission scans are needed and the attenuation is assumed to be uniform for small animals such as mice. However, this can be shown to be an oversimplification.

Potential benefits of the CT-based attenuation correction method over the PET-based method include: (1) reduction of crosstalk from PET annihilation photons at low x-ray energies during post-injection transmission studies; (2) lower statistical noise in transmission images acquired on CT versus PET; (3) availability of high-quality anatomical information; and (4) higher throughput imaging protocol.

In this work, we adapt an existing CT-based attenuation correction algorithm (Kinahan *et al* 1998) used on clinical PET/CT scanners to our preclinical small animal PET and CT scanners.

2. Materials and methods

For all studies, the PET data were acquired with a microPET® Focus™ tomograph (Tai *et al* 2005) (CTI Concorde Microsystems Inc., Knoxville, TN). The energy window was 250–700 keV and the coincidence timing window was 6 ns. A 10 h emission normalization scan in coincidence mode and a 10 h blank scan in singles mode (60 passes of the point source mechanism, $\sim 4 \times 10^{10}$ total counts) were acquired using a 17 MBq (0.47 mCi) spiraling ^{68}Ge point source. All listmode data were sorted into 3D sinograms using a span of 3 and a ring difference of 47. All sinograms were Fourier rebinned into 2D sinograms prior to reconstruction. Images were reconstructed using 2D filtered backprojection with a ramp filter cutoff at the Nyquist frequency resulting in an isotropic spatial resolution of 1.7 mm full width at half maximum (FWHM). In addition to attenuation, the emission data were corrected for detector efficiency, random coincidences, deadtime and photon scatter (Watson 2000).

For all studies, the CT data were acquired with a MicroCAT™ II tomograph (ImTek Inc., Knoxville, TN). The x-ray tube was biased at 70 kVp and had 2 mm of added aluminium filtration. The exposure time was 500 ms per projection and tube current was 500 μA. The angular sampling was $1°$ per projection for a full $360°$ scan. The x-ray detector of this system is rectangular (2 k × 3 k) and can image the whole body of a mouse in a single rotation. Images were reconstructed using the Feldkamp cone-beam algorithm for filtered backprojection with a ramp filter cutoff at the Nyquist frequency. The CT data were not corrected for scatter or beam hardening artefacts. This system's x-ray detector can also be rotated by $90°$ to image a rat with a larger diameter field of view.

2.1. Attenuation correction methods

2.1.1. Scaling method. After acquisition and reconstruction of microPET emission data, a single global scale factor was applied to the images to compensate for attenuation. This method assumes a cylindrical subject with uniform attenuation. For phantoms, this scale factor was
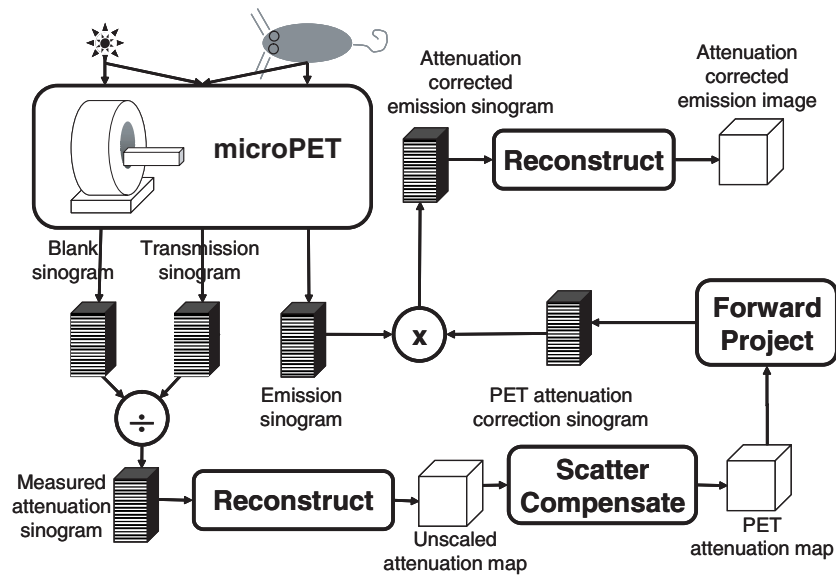
Figure 1. A flow chart of the steps involved in the PET-based attenuation correction for microPET.

calculated from theoretical values. For a 3.0 cm diameter cylindrical, water-filled phantom, the theoretical scale factor is 1.33. For animal subjects, this scale factor was calculated by converting the animal into a cylinder of water. Thus, a 35 g mouse, 8 cm long from snout to base of tail, is converted to a cylinder with a diameter of 2.4 cm. Although annihilation photons will travel through different amounts of material through the uniform, cylindrical object, this method applies the maximum correction factor to all lines of response.

2.1.2. PET-transmission (PET-TX) method. The PET-based method of attenuation correction is described here and illustrated in figure 1. In previous work (Chow *et al* 2002a), we have confirmed that PET transmission images for small animal tomographs were best acquired in singles mode (Karp *et al* 1995). Following emission and transmission acquisition, the listmode data were histogrammed into sinograms. The counts in the blank and transmission sinograms were normalized for acquisition time. Attenuation correction sinograms were created by calculating the ratio of the blank and transmission sinograms. Transmission images were reconstructed from the natural logarithm of these attenuation correction sinograms. These transmission images were compensated for photon scatter by scaling the measured linear attenuation coefficient (LAC) to the theoretical value for 511 keV photons (Dekemp and Nahmias 1994). New attenuation correction sinograms were created by forward projection through this corrected transmission image.

2.1.3. CT-transmission (CT-TX) method. Previously (Chow *et al* 2002b), we described the CT-based correction method using a previous generation of microPET and microCT scanners. The CT-based method of attenuation correction for the current generation of tomographs is described here and illustrated in figure 2. Following acquisition of PET and CT data using an imaging chamber (Stout *et al* 2003) that mounts onto the two separate systems, the microCT image is aligned to the microPET field of view using a predetermined, geometric transformation matrix. This transformation matrix is created from a manual alignment of
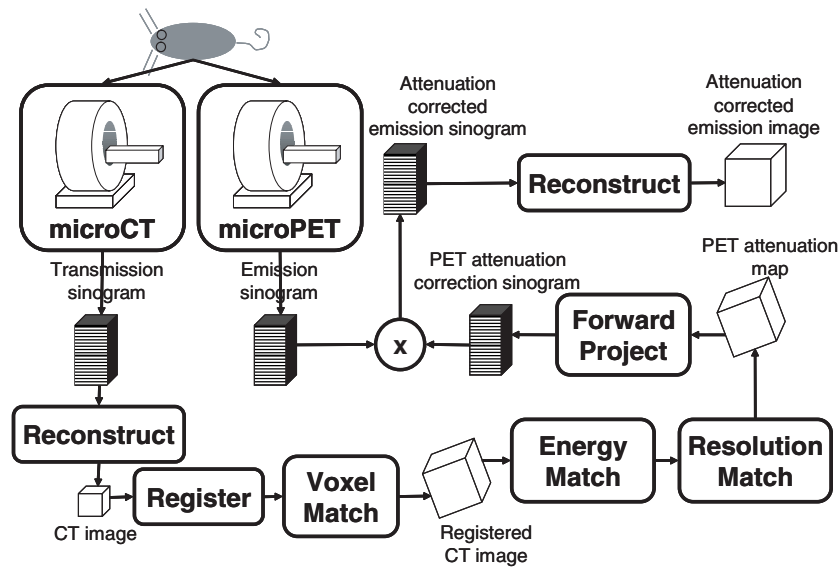
Figure 2. A flow chart of the steps involved in the CT-based attenuation correction for microPET.
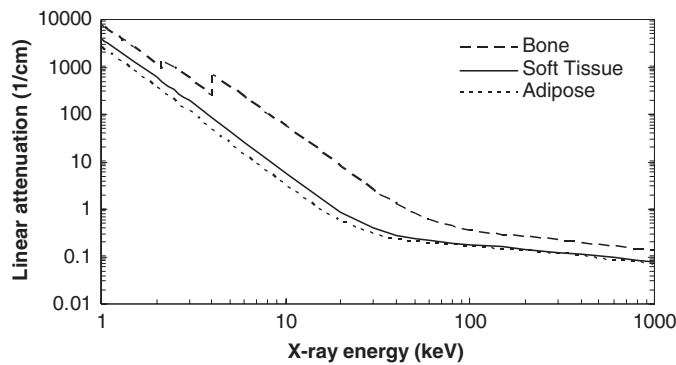

Figure 3. Energy dependence of linear attenuation coefficients for different tissues. CT photon energy from 10 to 70 keV; PET annihilation photon energy 511 keV. Data from Hubbell and Seltzer (2001).

microPET and microCT scans of fiducial markers (Isotope Products Laboratories, Valencia, CA) using the Automated Image Registration software package (Woods *et al* 1993). The transformation of the registered CT transmission image to one for PET attenuation correction involves matching (1) the voxel size, (2) the photon energy and (3) the spatial resolution.

Next, the registered CT image needs to match the PET voxel size. This voxel matching step is conceptually combined with the alignment step in registration. However, for clarity, we consider the two procedures separately. After alignment of the two fields of view, the CT image is down sampled to match the PET image voxel size (e.g., from 0.2 mm cubic voxels to $0.4 \times 0.4 \times 0.8$ mm^3).

Subsequently, matching of the energy is required, since the CT attenuation map is acquired with a continuous x-ray spectrum ranging from 10 to 70 keV (average energy 40 keV) whereas those needed for PET are at 511 keV. Figure 3 shows the energy dependence of the LACs for
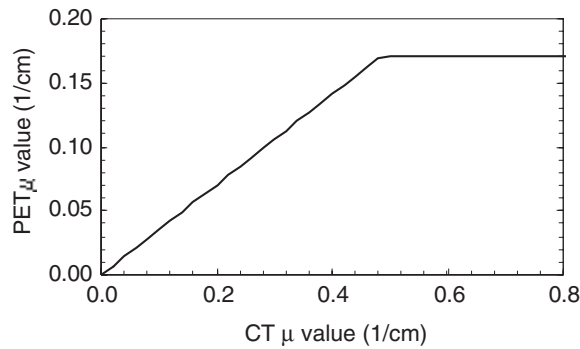
Figure 4. Mapping of linear attenuation coefficients from CT (average energy of 40 keV) to PET (511 keV) energy. Data calculated from Hubbell and Seltzer (2001).

Table 1. Tissue linear attenuation coefficients, CT versus PET. Data calculated from Hubbell and Seltzer (2001).

LAC (cm^{-1})	40 keV	Water scaled	511 keV
Adipose	0.228	0.080	0.090
Water	0.268	0.095	0.095
Soft tissue	0.285	0.100	0.099
Cortical bone	1.278	0.450/0.170[a]	0.170

[a] Threshold to 0.170 cm^{-1}.

different tissues (Hubbell and Seltzer 2001). The mapping of the LAC for tissue X to PET energy, $\mu_{\text{PET},X}$, is given by

$$\mu_{\text{PET},X} = \mu_{\text{CT},X} \times \frac{\mu_{\text{PET},H_2O}}{\mu_{\text{CT},H_2O}} \leqslant \mu_{\text{PET,bone}} \tag{1}$$

where $\mu_{\text{CT},X}$ is the LAC of material X measured by CT, μ_{CT,H_2O} is the LAC of water measured by CT, μ_{PET,H_2O} is the LAC of water at 511 keV and $\mu_{\text{PET,bone}}$ is the LAC of bone at 511 keV.

This mapping involves first scaling all tissues relative to the theoretical attenuation value of water at 511 keV, μ_{PET,H_2O}. The measured attenuation coefficient of water at CT energy, μ_{CT,H_2O}, is estimated by a volume of interest centred about the centre of mass of the imaged object. This volume about the centre of mass is assumed to be either soft tissue in animal studies or water in phantom studies. The CT image values, $\mu_{\text{CT},X}$, are thus rescaled relative to the theoretical value of water for PET. Table 1 lists the relevant LACs of select tissues at the average CT energy, at 511 keV, and values after mapping. As seen in table 1, the absorption of bone relative to water at low-CT energies is much higher than that at 511 keV. Therefore, a new maximum value can be set to the theoretical value for bone at 511 keV, $\mu_{\text{PET,bone}}$. A plot of the μ-mapping given by equation (1) is shown in figure 4.

After matching the voxel size and energy, the spatial resolution of the CT image is matched to the spatial resolution of the PET scanner (Chatziioannou and Dahlbom 1996). This step is typically combined with the forward projection step; however, for clarity in figure 2, we illustrate the two procedures separately. Now, the image is transformed into a PET attenuation map. A forward projection through this image generates the attenuation correction factors by summing up any attenuation in each line of response of the PET system.
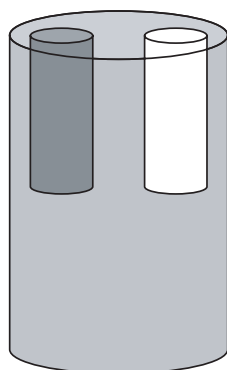
Figure 5. Schematic of the rat-sized compartment phantom. One of the chambers was empty, or air-filled, while the other chamber was filled with a solution whose activity concentration was 3.9 times that of the background chamber.

2.2. Phantom studies

Two phantom studies were performed to test the accuracy of the three attenuation correction methods outlined above. A 60 cc Monoject syringe (30 mm diameter filled to 30 cc) (Kendall Healthcare, Mansfield, MA) was used as a mouse-sized phantom. It was filled with 4.55 MBq (0.123 mCi) of [^{18}F]fluorodeoxyglucose (^{18}F-FDG).

A 51 mm diameter by 158 mm long cylinder was used as a rat-sized phantom. The phantom, illustrated in figure 5, has three separate fillable regions: a uniform background region containing two smaller cylindrical compartments (12.5 mm diameter). The uniform region was filled with 46.0 MBq (1.243 mCi) of ^{18}F-FDG while one of the smaller chambers was filled with 5.11 MBq (0.138 mCi) of ^{18}F-FDG. This resulted in the small chamber having an activity concentration 3.9 times higher than the background region. The other small chamber was not filled (air only).

For each phantom study, three scans were acquired:

(1) a 2 h PET emission scan with 5×10^8 and 2×10^9 counts for the mouse-sized and rat-sized phantom studies, respectively;
(2) a 20 min PET transmission scan in singles mode with $\sim 1.3 \times 10^9$ total counts during two passes of the point source mechanism after the radioactivity decayed overnight;
(3) a 10–20 min CT transmission scan to cover the same microPET field of view.

To compensate for photon scatter in the PET transmission scan, the mean in a large cylindrical volume of interest (VOI) that included most of the solution in the phantom was set to the theoretical LAC of water at 511 keV. A 22 mm diameter × 9.6 mm long VOI was drawn in the mouse-sized phantom data, while a 38 mm diameter × 9.6 mm long VOI was used for the rat-sized phantom.

To get microPET emission image values calibrated to the true activity concentration as measured by a scintillation well counter (Perkin-Elmer, Boston, MA), another phantom study was performed. A 60 cc, 39 mm diameter Nalgene bottle (Nalge Nunc International, Rochester, NY) was filled with 4.51 MBq (0.122 mCi) of ^{18}F-FDG. Emission data were acquired for 2 h; followed by a 10 min CT transmission dataset. After reconstruction, the CT image was segmented into materials with known PET attenuation coefficients (i.e., water, phantom wall and bed). Forward projection through this segmented image gave a sinogram with 'perfect', narrow beam attenuation correction factors. This image was also used as input for emission

scatter correction. The measured scintillation well counter concentration and the mean in a large cylindrical VOI (32 mm diameter $\times$ 9.6 mm long) drawn on the corrected emission image were used to convert emission image values to activity concentration.

The true activity concentration for each phantom study was determined by measuring four 45 μl samples of the radioactive solution in a scintillation well counter. The weight of the sample was measured using an analytical balance (Fisher Scientific International, Inc., Hampton, NH).

The above phantom studies were evaluated based on noise and accuracy. Noise analysis in both PET and CT transmission images was performed on images reconstructed from the 'PET attenuation correction sinograms' indicated in figures 1 and 2. Small, cylindrical VOIs were drawn in the uniform region of the phantoms. A 6.8 mm diameter $\times$ 14 mm long VOI was drawn in the mouse-sized phantom and a 9.5 mm diameter $\times$ 14 mm long VOI was drawn in the rat-sized phantom. The same VOIs were used to measure the noise in the PET emission images.

To evaluate the quantitative accuracy in the emission images, the same large VOIs drawn on the PET transmission images for scatter compensation were used on the PET emission images. Smaller VOIs (6.1 mm diameter $\times$ 9.6 mm long) were also drawn in the inner cylinders of the rat-sized phantom to compare against the measured activity concentration in the background compartment.

2.3. Animal studies

A 21 g C3H mouse (7.5 cm length) was kept under 2% isofluorane anesthesia and fitted with a catheter in the tail vein. Singles transmission data were acquired on the microPET® Focus™ first using the ^{68}Ge point source for 20 min (two passes of the point source mechanism, 1.3×10^9 total counts). The mouse was injected via the tail vein catheter with 7.45 MBq (0.201 mCi) of ^{18}F-FDG and dynamic emission data were acquired for 60 min. The listmode data were histogrammed into one frame with the first 40 min and a second frame with the remaining 20 min. Lastly, the mouse was scanned in the MicroCAT™ II for 10 min with 1 bed position. A VOI was drawn in the abdomen and used to calculate the PET transmission scatter compensation factor.

A 225 g Sprague–Dawley rat (18.5 cm length) was anaesthetized with 2% isofluorane and imaged in the CT scanner using two overlapping bed positions covering the heart and kidneys. The CT scan was acquired before PET to properly position the large animal and its bed in the 8 cm diameter CT field of view. Singles transmission data were subsequently acquired on the microPET® Focus™ using the ^{68}Ge point source for 20 min (two passes of the point source mechanism, 1.3×10^9 total counts). The rat was injected via the tail vein with 76.6 MBq (2.07 mCi) of ^{18}F-FDG and dynamic emission data were acquired for 60 min. The listmode data were histogrammed into one frame with the first 40 min and a second frame with the remaining 20 min. A VOI was drawn in the abdomen of the PET transmission image and used to calculate the PET transmission scatter compensation factor.

3. Results

3.1. Phantom studies

Table 2 summarizes the noise analysis (ratio of the standard deviation and the mean) of the transmission images for the two phantoms in the uniform region. Note that the CT attenuation maps have much less noise than the PET-derived maps.
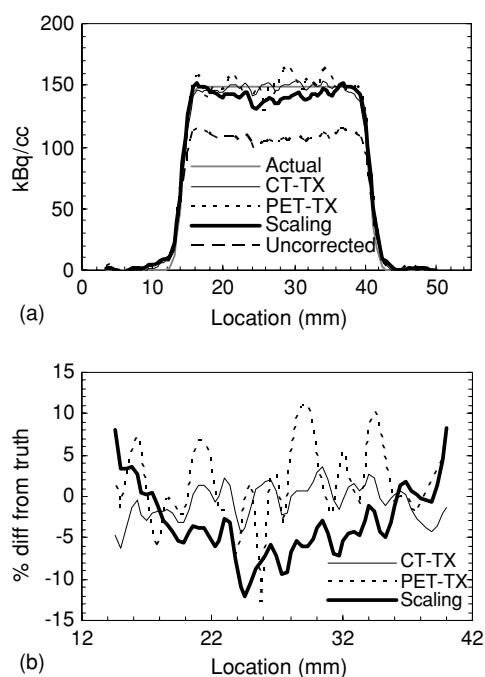
Figure 6. (a) Transverse microPET emission profiles through the centre of the mouse-sized phantom. (b) Per cent difference from truth for each method of attenuation correction.

Table 2. Relative noise (%) of the transmission images in the two phantoms studied.

Phantom	PET-TX	CT-TX
Mouse-sized	21.6	1.0
Rat-sized	23.6	1.8

Table 3. Relative noise (%) of the emission images in the two phantoms studied.

Phantom	Uncorrected	Scaling	PET-TX	CT-TX
Mouse-sized	4.1	4.1	6.3	3.6
Rat-sized	6.1	6.1	10.5	5.1

Table 3 summarizes the noise analysis of the emission images for the phantom studies. The measured noise in the emission image is reduced for both phantoms using the CT-based attenuation correction. Most likely, the uncorrected measurement included noise and systematic bias from the cupping artefact. With low-noise attenuation correction, the bias was removed, leaving the intrinsic noise of the emission image. For the PET-based method, the noise was higher in both phantom studies when compared to the uncorrected images. The increase in noise is attributed to the propagation of noise from the PET transmission data (Dahlbom and Hoffman 1987).

Figure 6(a) shows the transverse profile across the centre of the mouse-sized phantom image with the three methods of attenuation correction. Figure 7(a) shows the transverse profile across the centre of the rat-sized phantom for the three methods of attenuation correction in the uniform region. To better visualize the differences between each method, the per cent
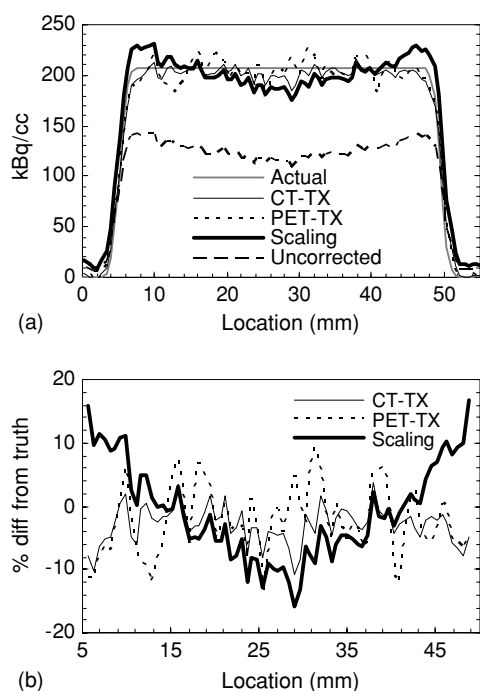
Figure 7. (a) Transverse microPET emission profiles through the uniform region of the rat-sized phantom. (b) Per cent difference from truth for each method of attenuation correction.
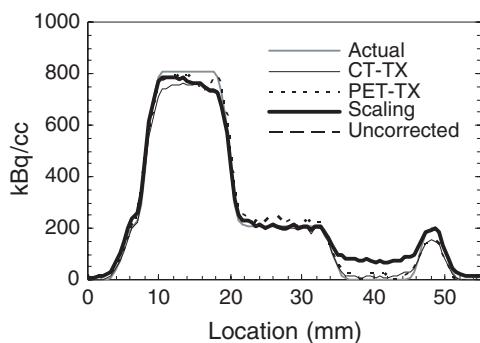

Figure 8. Transverse microPET emission profiles through the non-uniform region of the rat-sized phantom.

difference of each profile from the actual values is plotted in figures 6(b) and 7(b) over the non-zero region. Note the apparent 'horns' on the edges of the image produced with the scaling method of attenuation correction. Figure 8 shows the profiles in the non-uniform region. Note the bias in the air-only chamber in the 'Scaling' profile.

Table 4 summarizes VOI analysis in the non-uniform region of the rat-sized phantom. Attenuation correction (either PET- or CT-based) led to an improvement in the air to background ratio (from 0.36 to 0.06). The residual activity concentration in the air chamber of the 'Scaling' profile is attributed to scatter in the emission data since the manufacturer's implementation of the scatter correction requires an attenuation map. The difference among the three methods in the hot-chamber-to-background ratio is not statistically significant.
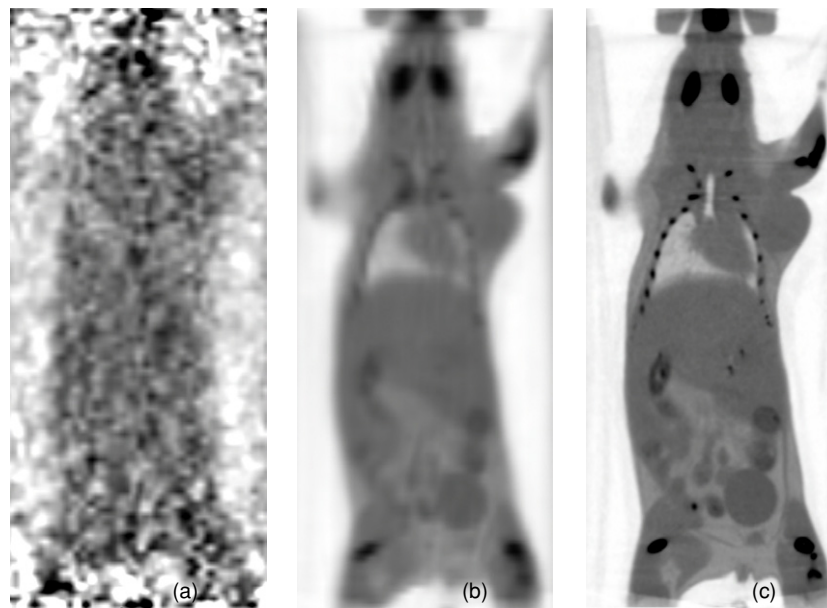
Figure 9. Coronal transmission images at the level of the mouse heart. (a) PET transmission, (b) CT transmission blurred to microPET resolution and (c) original unblurred CT transmission.

Table 4. ROI analysis in the non-uniform region of the emission images for the rat-sized phantom.

Ratio	Uncorrected	Scaling	PET-TX	CT-TX	True
Air/background contrast	0.36 ± 0.06	0.36 ± 0.06[a]	0.06 ± 0.08	0.06 ± 0.05	0.00
Hot/background contrast	3.73 ± 0.26	3.73 ± 0.26	3.82 ± 0.39	3.74 ± 0.19	3.89

[a] Significant difference from true ratio.

Table 5. Accuracy of the activity concentration (% difference from expected) in the corrected microPET images.

Phantom	Uncorrected	Scaling	PET-TX	CT-TX
Mouse-sized	−26.4	−2.5	+1.5	−0.1
Rat-sized	−38.5	−0.4	−1.9	−2.6

Table 5 tabulates the accuracy of the measured activity concentration for each of the three methods in the uniform regions of the two phantoms. The accuracy is computed as the per cent difference between the calibrated microPET emission image values in a large ROI and the calibrated scintillation well counter measurements. Note that performing attenuation correction significantly improves the quantitative accuracy of microPET images.

3.2. Animal studies

Figure 9 shows coronal slices through the PET and CT transmission images used for attenuation correction of the mouse study plus the original CT image. In the CT-based method, note that emission images are corrected using low-noise images shown in figure 9(b) and fused with high-resolution anatomical images shown in figure 9(c). Figure 10 shows profiles through the mouse heart and kidneys during the second dynamic frame for the three correction methods.
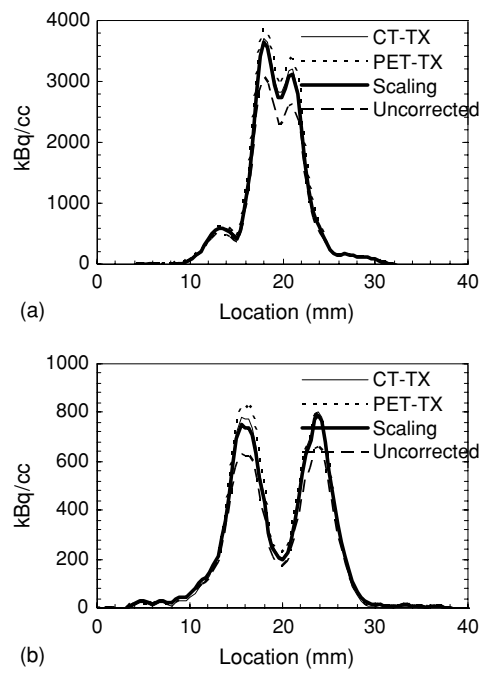
Figure 10. Transverse microPET emission profiles through (a) the mouse heart and (b) the kidneys with the three methods of attenuation correction. Profiles from second dynamic frame summing the last 20 min of the scan, 40 min post-injection.
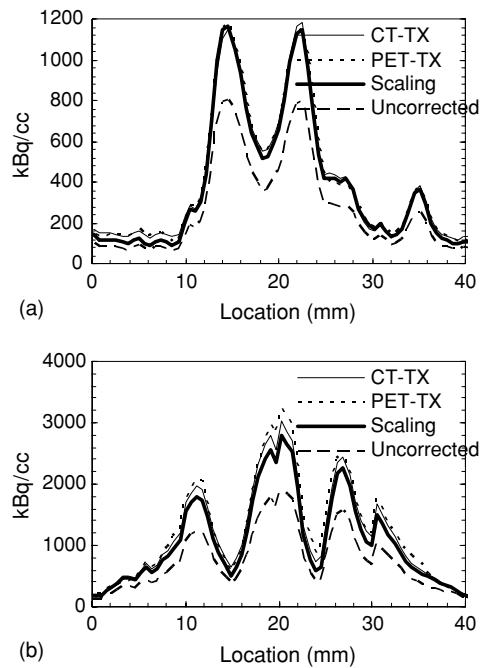

Figure 11. Transverse microPET emission profiles through (a) the rat heart and (b) the kidneys with the three methods of attenuation correction. Profiles from second dynamic frame summing the last 20 min of the scan, 40 min post-injection.

Figure 11 shows the profiles through the rat heart and kidneys during the second dynamic frame for the three correction methods.

4. Discussion and conclusions

Attenuation correction using the single scale factor method is quick and convenient but may lead to errors. Since the calculated scale factor does not account for the extra attenuation from the bed, this method tends to underestimate the amount of attenuation in the field of view. Although the accuracy of this method of attenuation correction seems promising as shown in table 5, the ROI included the entire cupping artefact caused by attenuation. As seen in the phantom profiles, the scaling method of attenuation correction does not remove the cupping artefact in the emission image. This is due to the fact that we are applying the same correction factor to all lines of response; however, not all lines of response will travel through the same amount of material. Only in a homogeneous, mouse-sized phantom can this bias be visualized, see figure 6. This error is more clearly visualized in larger phantoms (figure 7). The apparent efficacy of this attenuation correction method in *in vivo* studies depends on how well one manages to position the subject to resemble a cylinder and on how well the location where the profile is drawn has a similar diameter as the assumed cylinder.

If there is no subject motion, the main advantage of the PET-based method is that emission and transmission images are fully co-registered. However, the disadvantages of PET-based attenuation correction include: (1) noisy transmission images despite lengthy acquisitions (Dahlbom and Hoffman 1987, Chow *et al* 2002a); and (2) scattered photons cause inaccuracies in the measured attenuation coefficients at 511 keV. The propagation of the transmission noise into the emission data was also observed from table 3, where the noise in the rat-sized phantom increased from 6.1% in the uncorrected emission image to 10.5% in the PET-based attenuation correction method. In addition, the PET-based implementation of attenuation correction in living subjects is more complicated for post-injection scans (Smith *et al* 1994). This method significantly lengthens the total scan time and the animal's anesthesia exposure.

The primary advantage of the CT-based method is that low-noise, high-resolution anatomical maps (useful in PET signal localization) can be acquired in a short amount of time, compared to PET transmission maps. Another advantage of this method is the opportunity to perform uncomplicated post-injection transmission scans. Thus, with optimization of the CT scan protocol (Chow and Chatziioannou 2004), acquisition of a whole mouse for CT-based attenuation correction is flexible. The animal can be scanned in 5 min either during the uptake of the radiotracer or immediately after the PET emission scan. However, disadvantages of the CT-based method include: (1) inaccuracies co-registering the separately acquired emission and transmission images; (2) inaccuracies in converting tissue attenuation coefficients from an average CT energy to 511 keV; (3) image artefacts (such as beam hardening) propagating into the emission image; and (4) radiation dose (Cherry 2004).

The accuracy of the image registration is crucial in any method of attenuation correction. Registration accuracy for PET/CT imaging has been estimated to be better than 1 mm from fiducial marker studies (Stout *et al* 2003). Misalignment causes inaccurate image values at tissue interfaces.

Despite the lack of a water correction for beam hardening, the PET emission images corrected with the CT-based method were as accurate as those corrected with the PET-based method. For the rat-sized water phantom, the CT-based method included a 13% cupping artefact from beam hardening. This was estimated to create at most a 3% inaccuracy in the

attenuation correction factors. The beam hardening artefact did not create a noticeable artefact in the attenuation corrected emission image.

One drawback of the current implementation of the CT-based correction method is that we assume there are essentially two materials (soft tissue and bone) in the image. The attenuation coefficients for other tissues and materials such as trabecular bone, fat and CT contrast agents will be incorrectly mapped to PET energy. For example, the current implementation will underestimate the LAC of adipose tissue by $\sim$11%. Further work is needed to include these additional materials into a full attenuation correction.

The findings mentioned in this paper can be summarized as: (1) attenuation correction is important in quantitative PET in small animal subjects regardless of the method; (2) scaling is only a first-order correction method and should be avoided if possible in phantom and animal studies; and (3) the CT-based method of correction is superior to the PET-based method in terms of transmission noise propagating into the corrected emission image.

Acknowledgments

References

Chatziioannou A and Dahlbom M 1996 Detailed investigation of transmission and emission data smoothing protocols and their effects on emission images *IEEE Trans. Nucl. Sci.* **43** 290–4

Cherry S R 2004 *In vivo* molecular and genomic imaging: new challenges for imaging physics *Phys. Med. Biol.* **49** R13–48

Chow P L, Bai B, Siegel S, Leahy R M and Chatziioannou A F 2002a Transmission imaging and attenuation correction for the microPET® P4 tomograph 2002 *IEEE Nuclear Science Symp. Conf. Record (Norfolk)* vol 2 (Piscataway: IEEE) pp 1298–302

Chow P L and Chatziioannou A F 2004 Optimization of CT acquisition parameters for microPET/microCT imaging *Mol. Imaging (Saint Louis)* vol 3 (Cambridge: MIT Press) p 259

Chow P L, Rannou F R and Chatziioannou A F 2002b Attenuation correction for a 3D small animal PET tomograph, using x-ray microCT *Mol. Imaging Biol. (San Diego)* vol 4 (New York: Elsevier) p S17

Dahlbom M and Hoffman E J 1987 Problems in signal-to-noise ratio for attenuation correction in high-resolution PET *IEEE Trans. Nucl. Sci.* **34** 288–93

Dekemp R A and Nahmias C 1994 Attenuation correction in PET using single-photon transmission measurement *Med. Phys.* **21** 771–8

Huang S-C, Hoffman E J, Phelps M E and Kuhl D E 1979 Quantitation in positron emission computed-tomography: 2. effects of inaccurate attenuation correction *J. Comput. Assist. Tomogr.* **3** 804–14

Hubbell J H and Seltzer S M 2001 *Tables of X-ray Mass Attenuation Coefficients and Mass Energy-Absorption Coefficients* (version 1.3) (Gaithersburg: NIST) http://physics.nist.gov/xaamdi [Accessed 21 October 2001]

Karp J S, Muehllehner G, Qu H and Yan X-H 1995 Singles transmission in volume-imaging PET with a Cs-137 source *Phys. Med. Biol.* **40** 929–44

Kinahan P E, Townsend D W, Beyer T and Sashin D 1998 Attenuation correction for a combined 3D PET/CT scanner *Med. Phys.* **25** 2046–53

Smith R J, Karp J S and Muehllehner G 1994 Post injection transmission scanning in a volume imaging PET camera *IEEE Trans. Nucl. Sci.* **41** 1526–31

Stout D B, Chow P L, Gustilo A, Grubwieser S and Chatziioannou A F 2003 Multimodality isolated bed system for mouse imaging experiments *Mol. Imaging Biol. (Madrid)* vol 5 (New York: Elsevier) pp 128–9

Tai Y-C, Ruangma A, Rowland D, Siegel S, Newport D F, Chow P L and Laforest R 2005 Performance evaluation of the microPET (R) Focus: a third generation microPET scanner dedicated to animal imaging *J. Nucl. Med.* **46** 455–63

Watson C C 2000 New, faster, image-based scatter correction for 3D PET *IEEE Trans. Nucl. Sci.* **47** 1587–94

Woods R P, Mazziotta J C and Cherry S R 1993 MRI–PET registration with automated algorithm *J. Comput. Assist. Tomogr.* **17** 536–46

Zaidi H and Hasegawa B 2003 Determination of the attenuation map in emission tomography *J. Nucl. Med.* **44** 291–315